

ORIGINAL RESEARCH

UAV hyperspectral and lidar data and their fusion for arid and semi-arid land vegetation monitoring

Temuulen T. Sankey¹ , Jason McVay¹, Tyson L. Swetnam², Mitchel P. McClaran², Philip Heilman³ & Mary Nichols³

¹School of Informatics, Computing and Cyber Systems, Northern Arizona University, Flagstaff, Arizona

²School of Natural Resources and the Environment, University of Arizona, Tucson, Arizona

³USDA Southwest Watershed Research Center, Agricultural Research Service, Tucson, Arizona

Keywords

3D modeling, high-resolution DEM, lidar, species identification, UAV, vegetation monitoring

Correspondence

Temuulen T. Sankey, School of Informatics, Computing, and Cyber Systems, Northern Arizona University, PO Box 5693, Flagstaff, AZ 86011. Tel: 1 928 523 7098; Fax: 1 928 523 2300; E-mail: Temuulen.Sankey@nau.edu

Funding Information

This material is based on work supported by the U.S. Department of Agriculture, Agricultural Research Service, under Agreement No. 58-2022-5-13. The Woolpert Inc. manned aerial lidar data for WGEW was funded by ARS under USGS Contract Number G10PC00057S. Support was also provided by Northern Arizona University and the University of Arizona Agricultural Experiment Station.

Editor: Nathalie Pettorelli
Associate Editor: Ned Horning

Received: 30 November 2016; Revised: 6 February 2017; Accepted: 27 February 2017

doi: 10.1002/rse2.44

Remote Sensing in Ecology and Conservation 2018, **4** (1):20–33

Introduction

Ecological research requires a detailed and current inventory of the natural resources and environmental variables that control the phenomena in question. Baseline and comparative topographic and vegetation models are critical components in most common ecological research especially

Abstract

Unmanned aerial vehicles (UAVs) provide a new research tool to obtain high spatial and temporal resolution imagery at a reduced cost. Rapid advances in miniature sensor technology are leading to greater potentials for ecological research. We demonstrate one of the first applications of UAV lidar and hyperspectral imagery and a fusion method for individual plant species identification and 3D characterization at submeter scales in south-eastern Arizona, USA. The UAV lidar scanner characterized the individual vegetation canopy structure and bare ground elevation, whereas the hyperspectral sensor provided species-specific spectral signatures for the dominant and target species at our study area in leaf-on condition. We hypothesized that the fusion of the two different data sources would perform better than either data type alone in the arid and semi-arid ecosystems with sparse vegetation. The fusion approach provides 84–89% overall accuracy (kappa values of 0.80–0.86) in target species classification at the canopy scale, leveraging a wide range of target spectral responses in the hyperspectral data and a high point density (50 points/m²) in the lidar data. In comparison, the hyperspectral image classification alone produced 72–76% overall accuracies (kappa values of 0.70 and 0.71). The UAV lidar-derived digital elevation model (DEM) is also strongly correlated with manned airborne lidar-derived DEM ($R^2 = 0.98$ and 0.96), but was obtained at a lower cost. The lidar and hyperspectral data as well as the fusion method demonstrated here can be widely applied across a gradient of vegetation and topography to monitor and detect ecological changes at a local scale.

as they relate to ecological and environmental changes over time at various spatial and temporal scales. In particular, high-resolution topographic mapping and vegetation survey are fundamental first steps toward understanding many ecological, geologic, geomorphic, and hydrological processes (Guisan and Zimmermann 2000; Lee et al. 2002; Cook and Merwade 2009). Topographic and vegetation

mapping is largely accomplished using traditional field surveys (Fuller et al. 1998), which are time and labor intensive, and via satellite remote sensing (Xie et al. 2008), which provide coarse spatial and temporal resolution, or through manned aerial flights (Fensham and Fairfax 2002), which are expensive and difficult to acquire, especially in remote, rugged terrain which results in little or no temporal repeatability.

Unmanned aerial vehicles (UAVs) provide a new means to rapidly acquire detailed, site-specific inventory at a reduced cost and risk (Anderson and Gaston 2013) in finer spatial and temporal resolution, although UAV images typically cover a much smaller spatial extent due to limited flight time and in the USA due to the line of sight restrictions recommended by the Federal Aviation Administration (FAA). The costs per project will likely decrease as the instruments and UAV technology develop further, which would allow ecologists obtain high temporal resolution repeat data at a reduced cost.

Rapid advances in both active and passive sensor technology have enabled increased use of UAVs (Valavanis and Vachtsevanos 2015). UAV sensors enable image acquisition at centimeter (cm) spatial resolution and hourly–daily temporal resolutions (Rango et al. 2009; Harwin and Lucier 2012; Anderson and Gaston 2013; Javernick et al. 2014). The potential for generating high temporal and spatial resolution at intermediate scales (1–100 hectares) makes UAVs highly desirable for detailed and repeated measurements. UAV-derived data have been demonstrated to perform well in biodiversity monitoring and land-cover change detection (Koh and Wich 2012), precision agriculture (Hunt et al. 2010), hydrology and water resource management (DeBell et al. 2015), and detecting plant stress and pest infestation (Zarco-Tejada et al. 2012). UAV-derived vegetation indices such as normalized difference vegetation index (NDVI) have also been correlated with biophysical characteristics including leaf area index (LAI) and nitrogen uptake (Lelong et al. 2008).

The high spatial resolution of UAV data is of particular interest in ecological research in arid and semi-arid ecosystems, where vegetation patches are small and sparsely distributed, and are therefore difficult to detect via satellite remote sensing. Such data, for example, might allow detection of tall vegetation species with small canopies such as ocotillo (*Fouquieria splendens*) and columnar cacti including the saguaro cactus. Woody encroachment by creosote bush (*Larrea tridentate*) and mesquite (*Prosopis* spp), a topic that is widely studied in the south-western US (Grover and Musick 1990; Archer 1996; Aguiar et al. 1996; Brown and Carter 1998; Van Auken 2000; McClaran et al. 2008, 2010) is another example where the high-resolution data would be of great benefit. These processes have thus far been only documented via historical

aerial orthophotography and repeated ground measurements, acquired at less than annual and in some cases less than decadal time scales due to image acquisition costs. Satellite images can now be acquired for free at daily to biweekly intervals, but only at 10 m–1.1 km spatial resolution. Traditional field-based measurements, which offer the greatest precision, are time and cost intensive and only cover a limited spatial extent, which may not be representative of the entire watershed or landscape.

Light Detection and Ranging (lidar) is a commonly used active sensor for three-dimensional modeling of vegetation and the bare earth surface. Lidar-derived Digital Elevation Models (DEM) (Kraus and Pfeifer 2001; Sithole and Vosselman 2004), and vegetation Canopy Height Models (CHM) (St-Onge and Achaichia 2001; Lefsky et al. 2002; Popescu et al. 2002; Sankey et al. 2010) can now be generated in higher resolution from UAV-based sensors (James and Robson 2014). The higher-resolution data are expected to enable more detailed characterization of individual vegetation canopy structure as well as bare earth and microtopographic features, although UAV-based lidar data are still coarser resolution than most terrestrial laser scanner (TLS) data. The measurement capabilities of the newly available UAV-based lidar scanners have not been established and need to be demonstrated.

Hyperspectral sensors aboard UAV platforms represent another new sensor technology. Although manned airborne hyperspectral sensors have been successfully used to monitor vegetation, the relatively high cost of such image acquisition has limited its widespread application. Spaceborne hyperspectral sensors including Earth Observing-1 Hyperion provide another alternative with similar spectral resolution, but at a much coarser spatial resolution similar to Landsat data in 30 m pixels. Such spatial resolution has limited applications in arid land vegetation monitoring, especially at the species level, due to the sparse and patchy vegetation cover and distribution. In comparison, hyperspectral imagery acquired via UAVs offers much finer spatial resolution and avoid other complications associated with satellite data such as atmospheric effects and cloud cover.

A fusion of lidar and hyperspectral data leverages the synergistic nature of the vertical structure of vegetation and topography that can be estimated from lidar data and the horizontal estimates of vegetation and bare ground cover and composition that can be derived from the hyperspectral data. Previous efforts have integrated lidar derivatives with airborne hyperspectral data (Anderson et al. 2008; Dalponte and Bruzzone 2008; Swatantran et al. 2011) and satellite-borne multispectral imagery (Mundt et al. 2006; Wulder et al. 2009; Ke et al. 2010; Sankey and Glenn 2011). Specifically, lidar data have been fused in forested environments via regression and kriging

models with Landsat ETM+, Ikonos, and Quickbird imagery to improve classification accuracies (Hudak et al. 2002; Donoghue and Watts 2006; Mutlu et al. 2008), although some studies have reported marginal or no improvements in accuracies compared to lidar data alone (Hyde et al. 2006; Erdody and Moskal 2010). In rangelands, lidar fusion has resulted in greater improvement in classification accuracies (Sankey and Glenn 2011) because rangeland vegetation can be spectrally indistinguishable and lidar allows separation of varying vegetation based on the structural characteristics. A fusion of UAV-based lidar and hyperspectral images might further improve the previously documented benefits due to the finer spatial and spectral resolution of UAV data. A fusion of UAV-based lidar and hyperspectral images, however, has not been tested yet given the recent development of the UAV imaging platforms and limited payload capacity of most UAVs, which does not often allow deployment of multiple sensors per platform.

Objectives

In this study, we demonstrate an octocopter UAV equipped with a lidar scanner as well as a hyperspectral sensor and a fusion method in classifying vegetation at the species level at two long-term, experimental watershed sites in arid and semi-arid grassland and woodland ecosystems in the south-western US. The octocopter UAV is one of the first platforms permitted to operate in the US by the Federal Aviation Administration (FAA). Using the hyperspectral data, we first estimated presence and subpixel abundance of several different species including whitethorn acacia and creosote bush. Secondly, we estimated individual tree and shrub canopy height as well as herbaceous vegetation patch height using the lidar data. We also created a bare earth DEM in 0.5-m resolution. We then fused the hyperspectral classification outputs and lidar-derived vegetation canopy height estimates to produce a final land-cover-type map. We expected the fusion of lidar and hyperspectral images would offer particular advantages, especially in areas where multiple vegetation species of the same size class were found, where the species could be separated using the hyperspectral data, and in areas where spectral signatures between species were similar, but their sizes were different and can, therefore, be separated using the lidar data.

Materials and Methods

Study area

The study area was in Walnut Gulch Experimental Watershed (WGEW), a long-term United States Department of

Agriculture – Agricultural Research Service (USDA-ARS) experimental area located east of Tombstone, Arizona. Within the WGEW, we selected two sites encompassing the fetch footprint areas of two eddy covariance flux towers, which are part of the AMERIFLUX network: Kendall Grassland site (31.74°N, -109.93°W) and Lucky Hills Shrubland site (31.74° N, -110.05° W) (Heilman et al. 2008; Moran et al. 2008). The semi-arid desert Kendall Grassland site (Scott 2010) is dominated by Lehmann's lovegrass (*Eragrostis lehmanniana*), a non-native grass species, velvet mesquite (*Prosopis velutina*), yucca (*Yucca elata*), Mormon tea (*Ephedra trifurca.*), and ocotillo (*Fouquieria splendens*). The native grasses include curly mesquite (*Hilaria belangeri*), black grama (*Bouteloua eriopoda*), hairy grama (*Bouteloua hirsuta*), and three-awn (*Aristida hamulosa*) (Skirven et al. 2008). Lucky Hills is a Chihuahuan desert scrub site (Scott et al. 2006; Scott 2010), where the vegetation is dominated by creosote bush (*Larrea tridentate*), whitethorn acacia (*Acacia constricta*), tarbush (*Flourensia cernua*), mariola (*Parthenium incanum*), and littleleaf desert sumac (*Rhus microphylla*).

UAV platform and sensors

The octocopter UAV weighs 5.5 kg (Table 1) and was developed to carry an additional heavy payload of up to 6.5 kg (Service-Drone, Germany). The flight duration is relatively limited at 9 min per mission and covers approximately 800 m distance per flight. The octocopter is controlled via a hand-held remote control transmitter and a ground control station with navigation data link, which sends waypoint navigation information to the aircraft from a laptop computer. The octocopter carries a survey-grade Global Navigation Satellite System (GNSS) GPS and an inertial motion unit (IMU) inertial navigation system (INS) (SBG Systems North America, Inc., Chicago, IL), a HDL-32E lidar scanner (Velodyne Acoustics, Inc., Morgan Hill, CA), and a pushbroom hyperspectral nano-sensor with 272 spectral bands ranging 400–1000 μm (Headwall Photonics Inc., Fitchburg, MA). The GNSS GPS, IMU, lidar scanner, and hyperspectral sensor were all custom integrated with a data storage unit on a 2-axis gimbal (Fig. 1). This integration allows both sensors to simultaneously operate aboard the octocopter (Fig. 1).

Table 1. The UAV platform and sensor components.

Components	Location on the UAV platform	Weight (kg)
Hyperspectral sensor	2-axis gimbal	0.7 kg
Lidar scanner	2-axis gimbal	1.3 kg
GNSS and IMU	2-axis gimbal	0.3 kg
Data storage	2-axis gimbal	0.6 kg

UAV, unmanned aerial vehicles.



Figure 1. The octocopter unmanned aerial vehicle on the ground and in flight. On the two-axis gimbal is the integrated lidar scanner, hyperspectral sensor, a survey-grade Global Navigation Satellite System (GNSS) GPS, an inertial motion unit (IMU) inertial navigation system (INS), and data storage.

We simultaneously imaged each study site with both sensors. After each flight, the combined dataset is copied to the ground control station via the data link for pre-processing the lidar and hyperspectral data in a proprietary HyperSpecIII and SpectralView software (Headwall Photonics Inc., Fitchburg, MA), which integrate the GPS and IMU data to geometrically correct both images. The INS combines the IMU real-time inertial data with internal GPS information resulting in 2-cm RTK GNSS position accuracy at 200 Hz and 5 cm real-time autoadjusting heave. The INS also has its own internal data logger. The hyperspectral sensor can operate across a large range of flight altitudes, spatial resolution, and image extent depending upon flight altitude. The SpectralView software also converts the hyperspectral data into calibrated radiance, which is then imported into ENVI 5.3 and converted into reflectance and mosaicked for classification. After the initial pre-processing in the proprietary software, which all UAVs are commonly equipped with, all of the image analysis was performed in ENVI 5.3.

The Velodyne lidar scanner operates at up to 80–100 m maximum flight altitude and produces three-dimensional laser point cloud data with 32 laser beams/scan and ± 2 cm accuracy at 40° vertical field of view and 360° horizontal field of view. It is a single return lidar scanner with a laser spot coverage of 0.03 m^2 at each beam. The point density varies depending on flight speed. At a flight speed of 3 m/sec used in this study, average lidar point density was 50 points/m^2 .

Image acquisition and validation

Two UAV flight missions were completed at the Kendall Grassland site and one at the Lucky Hill site on October 8, 2015. Each flight path was represented by a rectangular area, $30 \times 180 \text{ m}$ in dimension (Fig. 2). The flights were performed at 70 m flight altitude and 3 m/sec flight speed close to solar noon in sunny weather conditions with

wind speed $<2 \text{ m/sec}$. Both hyperspectral and lidar data were acquired during each UAV flight.

To compare the UAV lidar data, manned aerial lidar data were acquired 3 weeks prior to the UAV survey at our study sites by Woolpert Inc. at USGS Quality Level 1 via a Leica ALS70-HP sensor with average point density $\sim 15 \text{ points/m}^2$ ($\leq 9.6 \text{ cm RMSE}_z$ at 95% CI). The 3-week difference in the timing of the manned and unmanned aerial flights was considered to be small with no measurable change in vegetation size and phenology. At our study sites, very little change in vegetation occurs in September, when rapid growth has passed and plants are beginning to slow metabolic function with decreased humidity and temperatures.

To validate the UAV hyperspectral data and to assess image classification outputs, plant canopies and target species of interest were geolocated and hand delineated using field-based GPS data, an independent source of high-resolution imagery, and ground-based photographs. Accuracy assessment samples were then randomly selected across the entire flight areas, but within these canopies, where the random samples are represented by individual pixels.

Lidar and hyperspectral image analysis and fusion

Following pre-processing, we imported all images into ENVI 5.3 image analysis software (Harris Corp, Bloomfield, CO) for analysis. Both the lidar and hyperspectral image analysis were performed in ENVI 5.3. The lidar point cloud data were processed by: (1) height filtering to separate ground versus non-ground vegetation returns in ENVI 5.3 (Sankey et al. 2013); <https://bcal.boisestate.edu/tools/lidar>, (2) delineating the points into individual woody vegetation canopies and herbaceous patches with X and Y location, Z-elevation (height), and canopy diameter estimates, which were derived via ENVI 5.3 Lidar

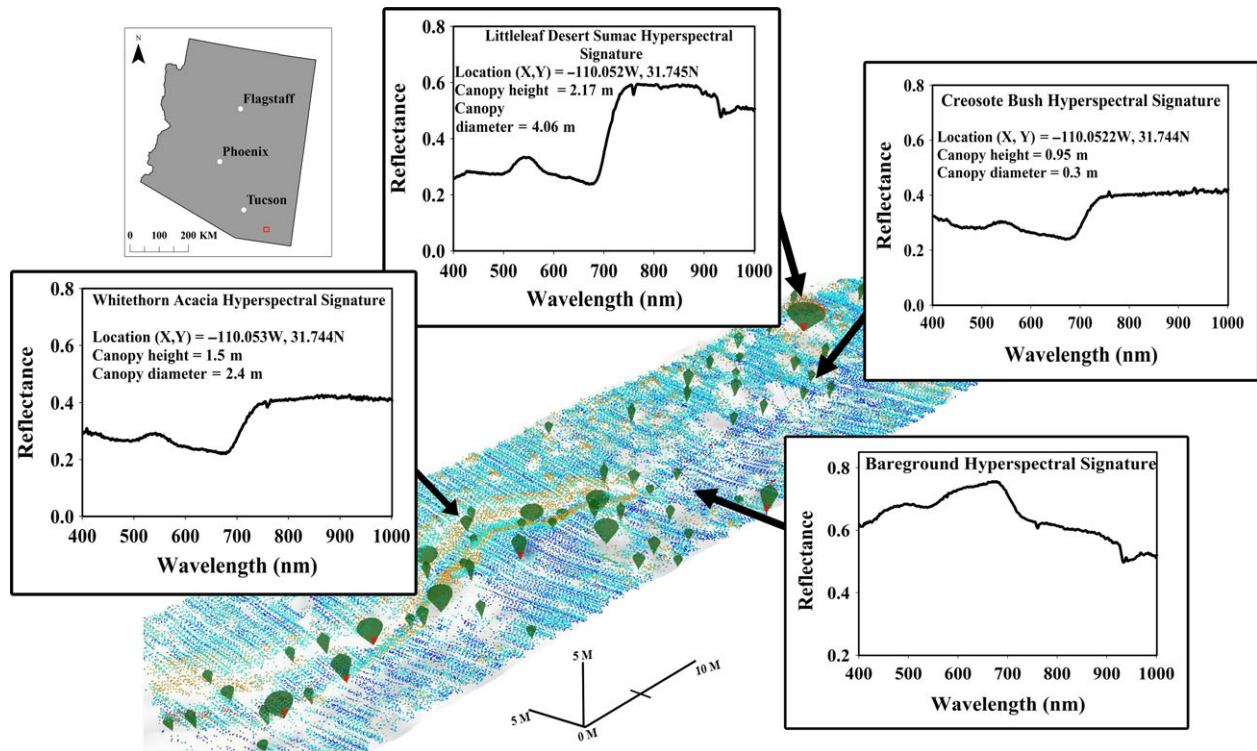


Figure 2. Unmanned aerial vehicle lidar point cloud (background image) and hyperspectral reflectance curve of some target species, including whitethorn acacia, littleleaf desert sumac, creosote bush, and bare ground at Lucky Hills study area (30.74°N, -110.05°W) at the United States Department of Agriculture – Agricultural Research Service (USDA-ARS) Walnut Gulch Experimental Watershed (WGEW), located east of Tombstone, Arizona (location indicated by a red box in the Arizona map inset). The background lidar point cloud shows ground returns and low-height vegetation returns in blue- and cyan-colored points. The taller vegetation points are shown as orange and red points and were used to derive 3D estimates of individual vegetation canopy height and diameter. The estimated vegetation canopy height and diameters are illustrated with respective sizes of green 3D shapefiles overlaid with the point cloud data.

module as a shapefile, and (3) rasterizing the bare earth digital elevation model (DEM) and a vegetation canopy height model (CHM) in 0.5-m resolution also in ENVI 5.3 Lidar module. Both the DEM and vegetation CHM were created as a raster only.

As a result, two different types of products were generated: (1) lidar point cloud that was classified into ground and vegetation canopies at the scale of individual plants (Fig. 2); this dataset retains the original high resolution of the lidar data and can be used for future high-resolution measurements for comparison and continued monitoring of the land surface and individual plants, and (2) a coarser-resolution raster datasets of DEM and CHM in 0.5-m cells. To assess the accuracy of the UAV lidar-derived DEM, we compared it to the conventional, manned aerial lidar-derived DEM via a simple regression model. Given the 15 points/m² density of the manned aerial lidar data, both DEMs were generated in 0.5-m resolution raster cells for this comparison, although the UAV lidar data had much finer resolution.

Using the hyperspectral data in ENVI 5.3, we classified the vegetation species via a mixture-tuned matched filtering sub-pixel analysis technique (Boardman 1998; Sankey et al. 2014), which identifies user-defined target species and estimates their abundances within each pixel in the image. Spectral mixture analysis techniques including the mixture-tuned matched filtering method are especially useful, where a mixture of vegetation species and bare ground is common within pixels. Although the UAV hyperspectral data had a fine spatial resolution of 6 cm, a mixture of herbaceous species, small shrubs, and bare ground was common at our study sites and a dominant cover within each pixel needed to be determined. In such conditions, linear spectral unmixing models are commonly used and produce a mixture which represents a linear combination of all the cover types and their respective areal coverage within each pixel (Rencz 1999). However, the mixture-tuned matched filtering method is recommended for mixed pixels with cover types having similar spectral signatures because it suppresses

background noise. Furthermore, the mixture-tuned matched filtering method is advantageous because it provides an estimate of false-positive detection of target cover (Boardman 1998). This sub-pixel classification technique was considered ideal in our study because: (1) it allows classification of user-defined target species and cover types of interest, and (2) it allows detection of a large number species and cover types given the many spectral bands available in the hyperspectral data (up to $n-1$ for the number of spectral bands) (Sankey et al. 2014). Using the target spectra, this classification approach matches the spectral signature in the image pixels to the known target spectral signature of each species. The result is an abundance estimate of each of the target species and cover types within each pixel. Given the small pixel size of the hyperspectral image (6 cm), we classified each pixel as a single cover type, if the target cover abundance estimate was >50% of the pixel. The target cover types at the Kendall sites were the dominant species of blue grama, velvet mesquite, Mormon tea, and yucca, whereas the target species at Lucky Hills included creosote bush, whitethorn acacia, mariola, and littleleaf desert sumac.

To leverage the synergistic opportunity provided by both the hyperspectral and lidar data in this study, we fused the hyperspectral image classification output with the lidar-derived plant height estimates. The fusion was performed via a decision tree classification approach, which was considered ideal because it allows merging of different types of data as well as data in varying spatial resolutions. Decision tree classification techniques have been widely tested in remote sensing applications. Decision tree classification performs equally compared to maximum likelihood, support vector machine-based methods, and random forest classification (Sharma et al., 2013). In a decision tree classification of remote sensing images, the target cover types are the response variables and the spectral bands can be the predictor variables. In our study, a separate decision tree was implemented at each study area to focus on the different target cover type at each study site and to leverage the lidar-derived height estimates along with the mixture-tuned matched filtering spectral unmixing outputs, which are as follows: (1) matched filtering (MF) scores that estimate the abundance of each species within each pixel, and (2) infeasibility values which represent the likelihood of false positives in the MF scores.

The decision tree structure is defined by a set of rules at decision nodes, where each rule further splits the dataset at each node (Sharma et al., 2013). This structure offered particular advantages in separating vegetation species that were similar either in spectral signature or height. The decision tree approach also provided an

opportunity to quantitatively combine the two estimates produced by the hyperspectral image classification outputs. While the mixture-tuned matched filtering classification reduces the 272 hyperspectral bands to two bands only, there is no direct method to combine these two bands to produce a final map of each species. Various user-defined approaches have been used thus far to quantitatively combine the two bands (Sankey et al., 2014). The decision tree classification merged the two images in addition to the lidar-derived vegetation canopy height models by defining a set of thresholds in the abundance estimates and their respective false likelihood values derived from the hyperspectral image. The decision tree rules were implemented for each pixel in the post-classification outputs of the hyperspectral and lidar data. The post-classification fusion approach was preferred for the decision tree classification because: (1) the individual classification of the hyperspectral and lidar data described above reduced the data size from 28,000 MB at each study site to 16 MB, (2) the individual classification of these datasets reduced the data dimensionality from 273 bands to 3 bands, and (3) the processing time was reduced from 45 min per study area to 45 sec, when the decision tree rules were implemented in ENVI IDL on a single desktop computer to simply merge the three bands only.

The decision tree rules defined for each target cover type a minimum abundance estimate (>30–50% in each pixel), a maximum false likelihood value (<25 in each pixel), and a threshold in canopy height estimates (<50 cm for all herbaceous species, 50 cm–2 m for shrub species). The dominant cover types of interest that we classified varied between the two sites. At Lucky Hills study site, for example, we classified whitethorn acacia, creosote bush, mariola, littleleaf desert sumac, and bare ground, whereas we classified mesquite, yucca, Mormon tea, blue grama, and bare ground at the Kendall site. A total of 100–1000 hyperspectral image pixels were used to derive the spectral signature for classification training for each target cover type at each site. These pixels were selected from known vegetation canopies, which were identified in the field and mapped with GPS locations, which were then georeferenced using a high-resolution terrestrial lidar-derived canopy height models.

To validate our classification results, 100–200 pixels for each target species at each site were randomly selected for accuracy assessment (Story and Congalton 1986). A separate accuracy assessment was performed for the classification of hyperspectral image alone and for the decision tree classification which fused the hyperspectral and lidar data together. From the accuracy assessment, an error matrix was generated for each of the two separate classification approaches to indicate an overall accuracy, a

producer’s accuracy, and a user’s accuracy (Story and Congalton 1986). The overall accuracy provides an estimate of the percent of total samples correctly classified across the entire study area samples. The producer’s accuracy estimates the percent of correctly classified samples for each cover type and is, therefore, independently calculated for each cover type. User’s accuracy is similarly calculated for each cover type and indicates the percent of samples that actually match the cover type on the ground (Story and Congalton 1986). We also calculated kappa statistics to evaluate the degree of agreement between the classification outputs and the field observations.

Results

The UAV lidar point cloud data had an average point density of 50 points/m² given the flight speed. The point

cloud data were successfully classified into ground versus vegetation returns (Fig. 2). The ground returns were then used to generate the DEM in 0.5 m resolution, which was strongly correlated with the commercial manned airborne lidar-derived DEM at both sites ($P < 0.001$, $R^2 = 0.98$ and 0.92 at Kendall and Lucky Hills site, respectively) (Fig. 3). The vegetation point cloud was also successfully used at both sites to delineate individual plant canopies along with estimates of their height and canopy diameter (Fig. 2). The vegetation canopy height models were then successfully fused with the hyperspectral image classification output.

The hyperspectral image had unique spectral signatures for the target species and cover types of interest in this study (Fig. 2). The hyperspectral image classification via matched filtering produced 76% overall accuracy (kappa value of 0.71) at the Lucky Hills site in 6 cm pixels.

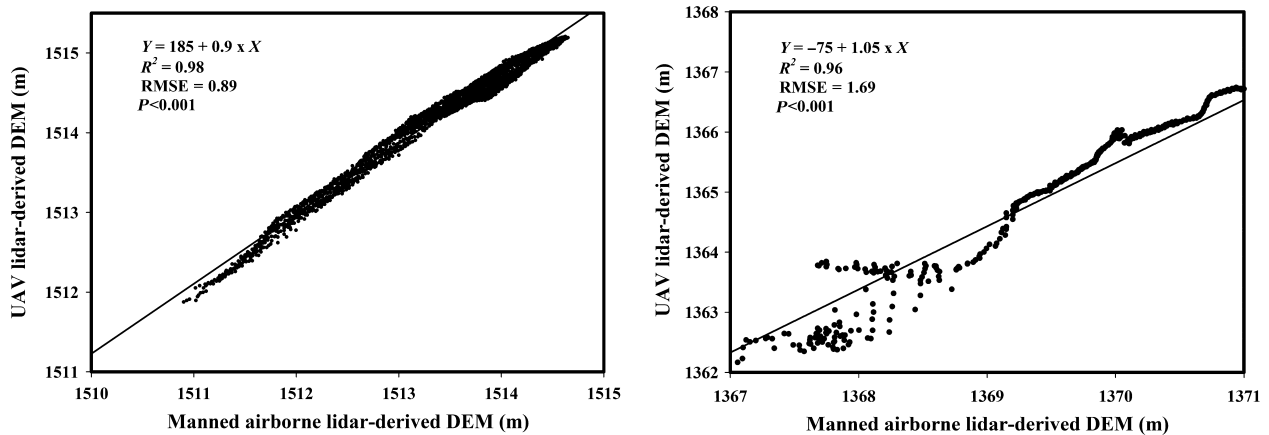


Figure 3. Comparison between the UAV lidar-derived and manned aerial lidar-derived DEM in 0.5 m resolution at the two study sites. The UAV lidar-derived DEM was very strongly correlated with the manned aerial lidar-derived DEM ($R^2 = 0.98$ and 0.96 at Kendall and Lucky Hill sites, respectively), which indicates that the UAV lidar provides an equally effective data source for generating high-resolution DEMs, but at a much lower cost. DEM, digital elevation models; UAV, unmanned aerial vehicles.

Table 2. Target vegetation species classification accuracies at the Lucky Hills study area via unmanned aerial vehicles hyperspectral image alone.

Classification	Reference data						Total # Samples	User’s accuracy
	Shadow/ unclassified	Bare ground	Mariola	Creosote bush	Littleleaf desert sumac	Whitethorn acacia		
Shadow/Unclassified	121	14		8		11	154	78%
Bare ground	14	231		6		18	269	86%
Mariola	90		110				200	55%
Creosote bush	18			188			206	91%
Littleleaf desert sumac	34			22	144		200	72%
Whitethorn acacia	28				32	132	192	69%
Total Samples	305	245	110	224	176	161	1,221	
Producer’s accuracy	66%	94%	100%	84%	82%	82%		
Overall accuracy								76%
Kappa								0.71

The accuracies were calculated using the values in the cells, which represent the number of randomly selected 6-cm pixels in each target cover class.

Producer's accuracies ranged 64–100%, whereas user's accuracies ranged 55–91% in the hyperspectral image classification alone (Table 2). Producer's accuracy tended to be consistently low for shadow pixels in the hyperspectral data. Given the small pixel size, many plant canopies had small shadows associated with them. The shadows tended to be mixed with other cover types leading to poor producer's accuracies in the hyperspectral data alone. Producer's accuracies for all the other classes, however, were very high, especially for bare ground and mariola. In comparison, user's accuracies were lower, particularly for mariola, whitethorn acacia, and littleleaf desert sumac due to many pixels within canopies that were classified as shadow.

The hyperspectral image classification at the Kendall grassland site produced 72% overall accuracy (kappa

value of 0.60) (Table 3). Producer's accuracies ranged 47–88%, whereas user's accuracies ranged 66–77%. Most of the low producer's and user's accuracies at this site were also associated with the shadow pixels within vegetation canopies (Table 3). Many canopies were accurately detected and at the correct locations, but each canopy included many pixels that were classified as shadows or were unclassified due to shadows. Mesquite and yucca had high producer's accuracies, but lower user's accuracies due to the shadows, whereas blue grama had high user's accuracy.

The overall accuracy was further improved to 89% at the Lucky Hills site (kappa value of 0.86) (Table 4), when the hyperspectral image was fused with the lidar data (Fig. 4). In the fusion-based final classification at the Lucky Hills site, producer's accuracies ranged 79–96%

Table 3. Target vegetation species classification accuracies at the Kendall grassland study area via unmanned aerial vehicles hyperspectral image alone.

Classification	Reference data					Total #Samples	User's accuracy
	Shadow/Unclassified	Mesquite	Yucca	Mormon tea	Blue grama		
Shadow/Unclassified	93		4	19	24	140	66%
Mesquite	35	85				115	71%
Yucca	8	11	55			74	74%
Mormon tea	32			76		106	70%
Blue grama	29		3		112	146	77%
Total Samples	197	96	62	95	136	581	
Producer's accuracy	47%	88%	88%	80%	82%		
Overall accuracy							72%
Kappa							0.64

The accuracies were calculated using the values in the cells, which represent the number of randomly selected 6-cm pixels in each target cover class.

Table 4. Target vegetation species classification accuracies at the Lucky Hills study area from the unmanned aerial vehicles lidar and hyperspectral image fusion via a decision tree classification.

Classification	Reference data						Total # Samples	User's accuracy
	Shadow/ Unclassified	Bare ground	Mariola	Creosote bush	Littleleaf desert sumac	Whitethorn Acacia		
Shadow/Unclassified	121	14		8		16	159	76%
Bare ground	14	231		6		18	269	86%
Mariola			181	3	8		192	94%
Creosote bush	6		14	199	11	9	239	83%
Littleleaf desert sumac			11		195		206	95%
Whitethorn acacia						165	165	100%
Total Samples	141	245	206	216	214		1230	
Producer's accuracy	86%	94%	88%	92%	96%	79%		
Overall accuracy								89%
Kappa								0.86

The accuracies were calculated using the values in the cells, which represent the number of randomly selected 6-cm pixels in each target cover class.

and user’s accuracies ranged 76–100% for the target cover species (Table 4). Among the target species, littleleaf desert sumac had the highest producer’s accuracy. The

fusion provided the greatest improvement in the classification of mariola, littleleaf desert sumac, and whitethorn acacia with producer’s accuracy increasing >30% for each. Many of the pixels within the canopies of these plants, which were previously classified as shadow in the hyperspectral image alone, were correctly classified in the fusion-based classification. This clearly indicates that the fusion leveraged vegetation canopy height information to eliminate many of the shadow pixels and include them in the plant canopy detection.

The overall accuracy at the Kendall grassland site was improved to 84% via the hyperspectral and lidar fusion (kappa value of 0.80) (Table 5). In this fusion model, producer’s accuracies ranged 67–83%. The user’s accuracies ranged 72–97% (Table 5). Similar to the Lucky Hills site, the fusion at the Kendall grassland site largely improved accuracies by reducing many of the pixels within canopies that were classified as shadow or were unclassified in the hyperspectral image classification alone. Producer’s accuracies in the fusion model were, therefore, greater specifically for mesquite, yucca, and Mormon tea, which benefited from the lidar-derived canopy height estimates.

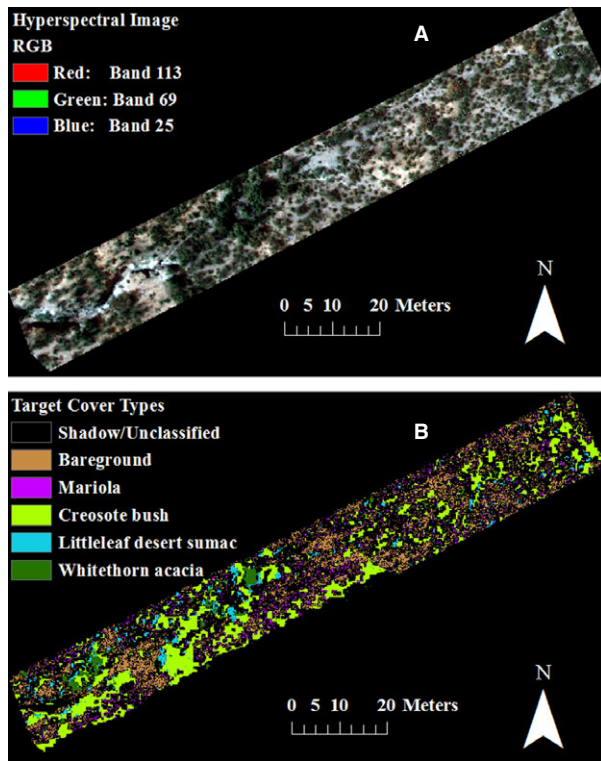


Figure 4. Unmanned aerial vehicles hyperspectral image displayed (Panel A) in true color composite using spectral band #25 at 451 nm wavelength, band #69 at 556 nm wavelength, and band #113 at 652 nm wavelength, and a lidar and hyperspectral image fusion-based classification output using the hyperspectral image and lidar data for the target cover types (Panel B) in Lucky Hills study area (30.74°N, -110.05°W) at the United States Department of Agriculture – Agricultural Research Service (USDA-ARS) Walnut Gulch Experimental Watershed (WGEW), east of Tombstone, Arizona.

Discussion

We leverage in this study two unique sources of data: a hyperspectral image with 272 spectral bands and three-dimensional lidar data. Fused together, the two data sources provide a unique capability to identify plant species and estimate their height, diameter, and volume at individual canopy scale and to accurately model earth surface in three dimension. At our study sites, the fusion offered particular advantages in identifying mesquite, Mormon tea, mariola, littleleaf desert sumac, and whitethorn acacia, which can be relatively similar in their spectral signature, but are different in height. Mariola is

Table 5. Target vegetation species classification accuracies at the Kendall grassland study area from the unmanned aerial vehicles lidar and hyperspectral image fusion via a decision tree classification.

Classification	Reference data					Total #Samples	User’s accuracy
	Shadow/Unclassified	Mesquite	Yucca	Mormon tea	Blue grama		
Shadow/Unclassified	93		2	9	24	128	72%
Mesquite	3	117				120	97%
Yucca	8	11	57			76	75%
Mormon tea	12			105		117	90%
Blue grama	22		3		119	144	83%
Total Samples	138	128	62	114	143	585	
Producer’s accuracy	67%	91%	92%	92%	83%		
Overall accuracy							84%
Kappa							0.80

The accuracies were calculated using the values in the cells, which represent the number of randomly selected 6-cm pixels in each target cover class.

shortest in height ranging 20–30 cm, whereas acacia, Mormon tea, and mesquite heights range between 100 and 180 cm and sumac 120–225 cm. The lidar data leveraged the height differences to improve the hyperspectral image classification. The synergistic benefit of the lidar-derived height estimate was especially evident for some species, including whitethorn acacia and creosote bush, which had very similar spectral reflectance in the hyperspectral data and as a result had very high producer's or user's accuracies in the hyperspectral image classification alone. Whitethorn acacia in Table 2, for example, had low user's accuracy, but a high producer's accuracy, which indicates that this species is overclassified with many false positives, likely at the cost of creosote bush being underclassified due to the spectral similarity. The height difference as detected by the lidar data, therefore, improved the separation between these two species. As demonstrated in Table 3, the producer's accuracy decreased for whitethorn acacia as a result of the fusion, whereas user's accuracy increased. The fusion better balanced the producer's and user's accuracies for these two species.

The hyperspectral image demonstrated here had very fine spectral and spatial resolution, which allowed individual plant species identification at the canopy scale. The many narrow spectral bands in the hyperspectral image, for example, can distinguish among whitethorn acacia and littleleaf desert sumac, as well as other cover types. A key advantage that the hyperspectral data with many narrow bands offer is the characterization of the reflectance and absorption features for each species at different wavelength locations across the spectral range. The high spectral resolution can potentially allow classification of many more species than classified here. The UAV hyperspectral image can also be used for invasive species detection similar to previous satellite-borne and manned airborne image-based efforts (O'Neill et al. 2000; Parker Williams and Hunt 2002; Dudek et al. 2004; Parker Williams and Hunt 2004; Root et al. 2004; Noujdina and Ustin 2008), but at a much greater temporal frequency to continuously monitor the spread of an invasive species. The hyperspectral data also offer a unique ability to spectrally distinguish other land surfaces such as bare ground and different types of geological parent material.

The UAV low flight altitude results in high spatial resolution data, which is particularly important in arid and semi-arid environments where vegetation is patchy and sparsely distributed. The small pixels enabled us to accurately identify individual plant canopies and small patches because the spectral mixing within each pixel is less than observed in larger pixels and spectrally pure pixels are more common. The hyperspectral data demonstrated here performed particularly well in detecting small patches of

blue grama, for example, which would typically be combined together with bare ground and shrubs in satellite data. Satellite image-derived vegetation classification and monitoring can be challenging as the vegetation covers a small fraction of each image pixel area, which ranges 900–250 000 m², for example, in Landsat and MODIS images. Similarly, ASTER satellite image-derived DEMs made commonly available by the US Geological Survey (USGS) are in 10-m resolution. The newly available Sentinel-2 satellite data are also acquired in 10-m resolution in the spectral bands 2, 3, 4, and 8. Although these spectral bands in Sentinel-2 provide much improvement in spatial resolution over Landsat and MODIS images, the 10-m resolution still does not readily allow species-level classification at the scale of individual plants. In contrast, the images demonstrated in this study have a spatial resolution that is orders of magnitude finer and can, therefore, substitute field-based measurements for Landsat and MODIS-based studies. The UAV lidar-derived DEM demonstrated in this study, for example, has 0.5-m resolution. The high spatial resolution in the UAV images allows subtle vegetation change detection over time such as phenological cycles, woody encroachment by mesquite and creosote bush, or die-off due to drought. The NEON Airborne Observation Platform (AOP) with its hyperspectral imager has a nominal resolution of 1.0 m (Kampe et al. 2010; Valavanis and Vachtsevanos 2015). In semi-arid ecosystems, even this spatial resolution can be too coarse to resolve small perennial herbaceous species which make up complex vegetation communities. The UAV hyperspectral imagery can be used to train the lower-resolution NEON AOP hyperspectral data as well as satellite image classification and to decipher complex spectral reflectance data with multispecies assemblages, where significant portions of the soil are exposed to the sensor. Similarly, many ecosystem-scale studies that leverage satellite data can use high-resolution UAV data as a means to train and validate their estimates. In such scenarios, high-resolution UAV data can replace ground-based measurements.

The UAV lidar data allow high-resolution three-dimensional estimates of individual plant canopies. Individual mesquite canopies, for example, can be delineated with estimates of their height and canopy diameter (Fig. 2). Such estimates can be used to measure total aboveground biomass (Sankey et al. 2013) and carbon using allometric relationships (Sankey et al. 2013), (McClaran et al. 2013). Furthermore, the UAV lidar-derived high-resolution DEM is very strongly correlated with manned airborne lidar-derived DEM. While the two DEMs compared in this study are generated in the same raster cell size, the UAV lidar point density is four times greater than that of the manned airborne lidar data. The increased point density is due to

several differences between the manned versus unmanned aerial lidar sensors including the greater number of lidar beams per scan (32 beams/scan) in the UAV lidar scanner, the lower flight speed (3 m/sec) of the UAV platform, which allows greater number of lidar scans per square meter area, and the larger field of view in the UAV scanner (40° vertical field of view and 360° horizontal field of view). The greater point density in the UAV lidar data can provide much more detailed estimates of earth surface processes and patterns for geomorphological and hydrological modeling, including soil erosion and gully erosion estimates and river channel morphology changes (Hutton and Brazier 2012).

Taken together, the high-resolution hyperspectral and lidar images from the UAV at the WGEW will become part of the long-term eco-physiological monitoring of the Lucky Hills and Kendall Grassland Flux sites. The hyperspectral signature characteristic of each species can serve as a benchmark high-resolution data which can be compared to later images to monitor plant vigor and stress. The three-dimensional structure of the vegetation derived from the UAV lidar will also help in establishing better estimates of evaporation/transpiration and carbon dioxide exchange at these sites. While the high-resolution benchmark images were acquired at a cost associated with the UAV instrument maintenance, future high-resolution images for continued monitoring, for example, can be acquired with more affordable means such as structure from motion.

The UAV images were acquired at a fraction of the potential cost of a manned aerial image acquisition (Table 6). While manned aerial lidar and hyperspectral image costs decrease with increasingly large areas to \$0.75–\$1.25/ha, manned airborne flight contracts often require a minimum area to be imaged bringing the typical cost of overflights to \$200,000–\$400,000 per project area, especially with rented sensor instruments. Individual scientists interested in small study areas with repeat images often cannot afford such datasets. UAVs provide a safer, more affordable, and robust imaging tool that can be deployed over a small target area at a cost of \$2,200–4,600 per project (\$25–\$50/ha) and at a high temporal resolution depending on the research needs.

Furthermore, the UAV platforms and sensor technology are rapidly changing, which further reduces the cost of UAV sensor deployment. We arrived at the cost estimates above given our calculations of instrument maintenance

requirements and their original prices. At the time of our instrument purchase in 2015, a fixed-wing UAV with a multispectral sensor cost approximately \$50,000, whereas lidar and hyperspectral sensors cost approximately \$30,000 and \$110,000, respectively. In the coming years, we expect the \$25–50/ha cost estimates to further decline. This will likely make UAV imaging a more desirable alternative for many scientists. The current limitations in the timing of UAV flights include weather conditions, especially wind speed, which impact flight stability and duration. UAV operational timing can also be influenced in the US by the acquisition of the Certificate of Authorization from the Federal Aviation Administration, such as the one used in this study because the UAV platform is a public aircraft. However, with proper planning and advanced notice, UAVs can be registered and authorized to fly for operation at a user-defined frequency and the Certificate of Authorization is no longer required for civil aircraft operations. This flexibility offers a large advantage over manned aerial imaging and satellite imagery. Most satellite imaging sensors have a fixed field of view at a routine schedule. Landsat satellite missions, for example, have 16-day re-visit time, which can often be reduced to 32-day intervals due to cloud cover. In contrast, UAV images can be acquired at weekly, daily, or even hourly intervals.

Summary and Conclusions

We present here performance assessment for an octocopter UAV, one of the first platforms permitted to operate in the US. The octocopter UAV equipped with a lidar scanner and hyperspectral sensor provides a large dataset with synergistic opportunities. Compared to the classification of hyperspectral data alone, the fusion of lidar and hyperspectral data provides >30% improvement in species identification by leveraging differences in plant height. Whereas the hyperspectral data provide high spatial and spectral resolution data, many pixels within canopies were unclassified or classified as shadow. The UAV lidar data improved accuracies by reducing these pixels. The UAV lidar data also provided accurate and high-resolution DEM much like the manned airborne lidar data. The lidar data capabilities need to be further tested for southwestern plant species such as the columnar cacti that are difficult to detect and map via coarser-resolution data

Table 6. Cost comparison (\$ US) between image acquisitions by conventional manned aerial platforms versus unmanned aerial vehicles (UAVs).

Imaging platforms	Lidar point density	Precision	Average area imaged/flight	Total average cost/project	Average cost/Ha
Manned aerial platforms	~15 points/m ²	20 cm	300 ha	\$300,000/project	\$1000/ha
UAVs	~50 points/m ²	10 cm	5.4 ha	\$3400/project	\$38/ha

from manned airborne and satellite remote sensing platforms. Other fusion methods to efficiently combine the lidar data with hyperspectral data need to be explored for ecological modeling and subtle environmental change detection such as individual plant growth and environmental degradation.

Ecologists and geoscientists across the world can take full advantage of these new research tools to overcome the spatial and temporal resolution of satellite-borne and manned airborne remote sensing at a significantly lower cost for local-scale studies. As the technology further develops, the costs of UAV images will likely decrease. Both the 2D imagery and 3D measurements can be used to model individual plants and resolve individual species spectral signatures, providing unprecedented level of detail. Such measurements can be linked with ecological process models that operate at high resolution over large areas. The detailed measurements also provide an effective means to link ground-based and in situ observations of small areal extent to coarser-resolution manned aerial and satellite-derived estimates.

Acknowledgments

This material is based on work supported by the U.S. Department of Agriculture, Agricultural Research Service, under Agreement No. 58-2022-5-13. The Woolpert Inc. manned aerial lidar data for WGEW was funded by ARS under USGS Contract Number G10PC00057S. Support was also provided by Northern Arizona University and the University of Arizona Agricultural Experiment Station. The authors wish to thank the United States Department of Agriculture – Agricultural Research Service WGEW researchers and staff for assisting with field work and for helpful review of the earlier draft of the manuscript and species identification. The authors also wish to thank the anonymous reviewers, who provided helpful suggestions and comments. The data used for conclusions in this study are included in the figures and tables in the manuscript. Any opinions, findings, conclusion, or recommendations expressed in this publication are those of the author(s) and do not necessarily reflect the view of the U.S. Department of Agriculture.

References

- Aguiar, M. R., J. M. Paruelo, O. E. Sala, and W. K. Lauenroth. 1996. Ecosystem responses to changes in plant functional type composition: an example from the Patagonian steppe. *J. Veg. Sci.* **7**, 381–390.
- Anderson, K., and K. J. Gaston. 2013. Lightweight unmanned aerial vehicles will revolutionize spatial ecology. *Front. Ecol. Environ.* **11**, 138–146.
- Anderson, J. E., L. Plourde, M. Martin, B. Braswell, M. Smith, R. Dubayah, et al. 2008. Integrating waveform lidar with hyperspectral imagery for inventory of a northern temperate forest. *Remote Sens. Environ.* **112**, 1856–1870.
- Archer, S. R. 1996. Assessing and interpreting grass-woody plant dynamics. Pp. 101–134 in J. Hodgson and A. W. Illius, eds. *The ecology and management of grazing systems*. CAB International, Wallingford, UK.
- Boardman, J. W. 1998. Leveraging the high dimensionality of AVIRIS data for improved sub-pixel target unmixing and rejection of false positives: mixture tuned matched filtering. Pp. 6 in: *Proceedings of AVIRIS 1998*. JPL, Pasadena, California.
- Brown, J. R., and J. Carter. 1998. Spatial and temporal patterns of shrub invasion in an Australian tropical grassland. *Landscape Ecol.* **13**, 93–102.
- Cook, A., and V. Merwade. 2009. Effect of topographic data, geometric configuration and modeling approach on flood inundation mapping. *J. Hydrol.* **377**, 131–142.
- Dalponte, M., and L. Bruzzone. 2008. Fusion of hyperspectral and lidar remote sensing data for classification of complex forest areas. *IEEE Trans. Geosci. Remote Sens.* **46**, 1416–1427.
- DeBell, L., K. Anderson, R. E. Brazier, N. King, and L. Jones. 2015. Water resource management at catchment scales using lightweight UAVs: current capabilities and future perspectives. *J. Unmanned Veh. Syst.* **3**, 1–24.
- Donoghue, D., and P. Watts. 2006. Using LIDAR to compare forest height estimates from IKONOS and Landsat ETM+ data in Sitka spruce plantation forest. *Int. J. Remote Sens.* **27**, 725–737.
- Dudek, K. B., R. R. Root, R. F. Kokaly, and G. L. Anderson. 2004. Increased spatial and temporal consistency of leafy spurge maps from multivariate AVIRIS imagery: a hybrid linear spectral mixture analysis/mixture-tuned matched filtering approach. In: *Proceedings of the 13th JPL Airborne Earth Science Workshop*; 21 March–2 April 2004. NASA Jet Propulsion Laboratory, Pasadena, CA.
- Erdody, T., and L. Moskal. 2010. Fusion of lidar and imagery for estimating forest canopy fuels. *Remote Sens. Environ.* **114**, 725–737.
- Fensham, R. J., and R. J. Fairfax. 2002. Aerial photography for assessing vegetation change: a review of applications and the relevance of findings for Australian vegetation history. *Aust. J. Bot.* **50**, 415–429.
- Fuller, R. M., G. B. Groom, S. Mugisha, P. Ipuleit, D. Pomeroy, A. Katende, et al. 1998. The integration of field survey and remote sensing for biodiversity assessment: a case study in the tropical forests and wetlands of Sango Bay, Uganda. *Biol. Cons.* **86**, 379–391.
- Grover, H. D., and B. Musick. 1990. Shrubland encroachment in southern New Mexico, USA: an analysis of desertification processes in the American Southwest. *Clim. Change* **17**, 305–330.

- Guisan, A., and N. E. Zimmermann. 2000. Predictive habitat distribution models in ecology. *Ecol. Model.* **135**, 147–186.
- Harwin, S., and A. Lucieer. 2012. Assessing the accuracy of georeferenced point clouds produced via multi-view stereopsis from unmanned aerial vehicle (UAV) imagery. *Remote Sens.* **4**, 1573–1599.
- Heilman, P., M. H. Nichols, D. C. Goodrich, S. N. Miller, and D. P. Guertin. 2008. Geographic information systems database, Walnut Gulch Experimental Watershed, Arizona, United States. *Water Resour. Res.* **44**, 5.
- Hudak, A., M. Lefsky, W. Cohen, and M. Berterretche. 2002. Integration of lidar and Landsat ETM+ data for estimating and mapping forest canopy height. *Remote Sens. Environ.* **82**, 397–416.
- Hunt, E. R., W. D. Hively, S. J. Fujikawa, D. S. Linden, C. S. Daughtry, and G. W. McCarty. 2010. Acquisition of NIR-green-blue digital photographs from unmanned aircraft for crop monitoring. *Remote Sens.* **2**, 290–305.
- Hutton, C., and R. Brazier. 2012. Quantifying riparian zone structure from airborne lidar: vegetation filtering, anisotropic interpolation, and uncertainty propagation. *J. Hydrol.* **442**, 36–45.
- Hyde, P., R. Dubayah, W. Walker, B. Blair, M. Hofton, and C. Hunsaker. 2006. Mapping forest structure for wildlife habitat analysis using multi-sensor (LIDAR, SAR/InSAR, ETM+, Quickbird) synergy. *Remote Sens. Environ.* **102**, 63–73.
- James, M. R., and S. Robson. 2014. Mitigating systematic error in topographic models derived from UAV and ground-based image networks. *Earth Surf. Proc. Land.* **39**, 1413–1420.
- Javernick, L., J. Brasington, and B. Caruso. 2014. Modeling the topography of shallow braided rivers using Structure-from-Motion photogrammetry. *Geomorphology* **213**, 166–182.
- Kampe, T. U., B. R. Johnson, M. Kuester, and M. Keller. 2010. NEON: the first continental-scale ecological observatory with airborne remote sensing of vegetation canopy biochemistry and structure. *J. Appl. Remote Sens.* **4**, 4351.
- Ke, Y., L. Quachenbush, and J. Im. 2010. Synergistic use of Quickbird multispectral imagery and LIDAR data for object-based forest species classification. *Remote Sens. Environ.* **114**, 1141–1154.
- Koh, L. P., and S. A. Wich. 2012. Dawn of drone ecology: low-cost autonomous aerial vehicles for conservation. *Trop. Conser. Sci.* **5**, 121–132.
- Kraus, K., and N. Pfeifer. 2001. Advanced DTM generation from LIDAR data. *Int. Arch. Photogrammetry Remote Sens. Spatial Infor. Sci.* **34**, 23–30.
- Lee, S., U. Chwae, and K. Min. 2002. Landslide susceptibility mapping by correlation between topography and geological structure: the Janghung area, Korea. *Geomorphology* **46**, 149–162.
- Lefsky, M. A., W. B. Cohen, G. G. Parker, and D. J. Harding. 2002. lidar Remote Sensing for Ecosystem Studies lidar, an emerging remote sensing technology that directly measures the three-dimensional distribution of plant canopies, can accurately estimate vegetation structural attributes and should be of particular interest to forest, landscape, and global ecologists. *Bioscience* **52**, 19–30.
- Lelong, C. C., P. Burger, G. Jubelin, B. Roux, S. Labbé, and F. Baret. 2008. Assessment of unmanned aerial vehicles imagery for quantitative monitoring of wheat crop in small plots. *Sensors* **8**, 3557–3585.
- McClaran, M. P., J. Moore-Kucera, D. A. Martens, J. van Haren, and S. E. Marsh. 2008. Soil carbon and nitrogen in relation to shrub size and death in a semi-arid grassland. *Geoderma* **145**, 60–68.
- McClaran, M. P., D. M. Browning, and C. Huang. 2010. Temporal dynamics and spatial variability in desert grassland vegetation. P. 166 in R. H. Webb, D. E. Boyer and R. M. Turner, eds. *Repeat photography: methods and applications in the natural sciences*. Island Press, 145.
- McClaran, M. P., C. R. McMurtry, and S. R. Archer. 2013. A tool for estimating impacts of woody encroachment in arid grasslands: allometric equations for biomass, carbon and nitrogen content in *Prosopis velutina*. *J. Arid Environ.* **88**, 39–42.
- Moran, M. S., C. D., Holifield Collins, D. C. Goodrich, J. Qi, D. T. Shannon, and A. Olsson. 2008. Long-term remote sensing database, walnut gulch experimental watershed, Arizona, United States. *Water Resour. Res.*, **44**, W05S10.
- Mundt, J., D. Streutker, and N. Glenn. 2006. Mapping sagebrush distribution using fusion of hyperspectral and lidar classifications. *Photogramm. Eng. Remote Sensing* **72**, 47–54.
- Mutlu, M., S. Popescu, C. Stripling, and T. Spencer. 2008. Mapping surface fuel models using lidar and multispectral data fusion for fire behavior. *Remote Sens. Environ.* **112**, 274–285.
- Noujdina, N. V., and S. L. Ustin. 2008. Mapping downy brome (*Bromis tectorum*) using multirate AVIRIS data. *Weed Sci.* **56**, 173–179.
- O'Neill, M., S. L. Ustin, S. Hager, and R. Root. 2000. Mapping the distribution of leafy spurge at Theodore Roosevelt National Park using AVIRIS. in R. D. Green, ed. *Proceedings of the Ninth JPL airborne earth science workshop*. NASA Jet Propulsion Laboratory, Pasadena, California.
- Parker Williams, A. E., and E. R. Hunt. 2002. Estimation of leafy spurge cover from hyperspectral imagery using mixture tuned matched filtering. *Remote Sens. Environ.* **82**, 446–456.
- Parker Williams, A. E., and E. R. Hunt. 2004. Accuracy assessment for detection of leafy spurge with hyperspectral imagery. *J. Range Manag.* **57**, 106–112.
- Popescu, S. C., R. H. Wynne, and R. F. Nelson. 2002. Estimating plot-level tree heights with lidar: local filtering with a canopy-height based variable window size. *Comput. Electron. Agric.* **37**, 71–95.
- Rango, A., A. Laliberte, J. E. Herrick, C. Winters, K. Havstad, C. Steele, et al. 2009. Unmanned aerial vehicle-based remote sensing for rangeland assessment, monitoring, and management. *J. Appl. Remote Sens.* **3**, 3542.

- Rencz, A. N. 1999. Pp. 251–307 *Remote sensing for the earth sciences*. Wiley and Sons, New York.
- Root, R. R., G. L. Anderson, S. N. Hager, K. E. Brown, K. B. Dudek, and R. F. Kokaly. 2004. Application of advanced remote sensing and modeling techniques for the detection and management of leafy spurge: challenges and opportunities. In: Proceedings of the Society for Range Management 57th Annual Meeting; 24–30 January, 2004; Salt Lake City, UT and Denver, CO, USA. Society for Range Management.
- Sankey, T., and N. Glenn. 2011. Landsat-5 TM and lidar fusion for sub-pixel juniper tree cover estimates in a western rangelands. *Photogramm. Eng. Remote Sensing* **77**, 1241–1248.
- Sankey, T. T., N. Glenn, S. Ehinger, A. Boehm, and S. Hardegree. 2010. Characterizing western juniper expansion via a fusion of landsat 5 thematic mapper and lidar data. *Rangeland Ecol. Manag.* **63**, 514–523.
- Sankey, T., R. Shrestha, J. B. Sankey, S. Hardegree, and E. Strand. 2013. lidar-derived estimate and uncertainty of carbon sink in successional phases of woody encroachment. *J. Geophys. Res. Biogeosci.* **118**, 1144–1155.
- Sankey, T., B. Dickson, S. Sesnie, O. Wang, and L. Zachmann. 2014. WorldView-2 high resolution improves desert invasive plant detection. *Photogramm. Eng. Remote Sensing* **80**, 193–885.
- Scott, R. L. 2010. Using watershed water balance to evaluate the accuracy of eddy covariance evaporation measurements for three semiarid ecosystems. *Agric. For. Meteorol.* **150**, 219–225.
- Scott, R. L., T. E. Huxman, W. L. Cable, and W. E. Emmerich. 2006. Partitioning of evapotranspiration and its relation to carbon dioxide exchange in a Chihuahuan Desert shrubland. *Hydrol. Process.* **20**, 3227–3243.
- Sharma, R., A. Ghosh and P. Joshi. 2013. Decision tree approach for classification of remotely sensed satellite data using open source support. *J. Earth. Syst. Sci.* **122**, 1237–1247.
- Sithole, G., and G. Vosselman. 2004. Experimental comparison of filter algorithms for bare-Earth extraction from airborne laser scanning point clouds. *ISPRS J. Photogramm. Remote Sens.* **59**, 85–101.
- Skirven, S., M. Kidwell, S. Biedenbender, J. P. Henley, D. King, C. H. Collins, et al. 2008. Vegetation data, walnut gulch experimental watershed, Arizona, United States. *Water Resour.* **44**, 5–8.
- St-Onge, B. A., and N. Achaichia. 2001. Measuring forest canopy height using a combination of lidar and aerial photography data. *Int. Arch. Photogrammetry, Remote Sens. Spatial Inform. Sci.* **34**, 131–138.
- Story, M., and R. G. Congalton. 1986. Accuracy assessment: a user's perspective. *Photogramm. Eng. Remote Sensing* **52**, 397–399.
- Swatantran, A., R. Dubayah, D. Roberts, M. Hofton, and J. Blair. 2011. Mapping biomass and stress in the Sierra Nevada using lidar and hyperspectral data fusion. *Remote Sens. Environ.* **115**, 2917–2930.
- Valavanis K. P., and G. J. Vachtsevanos (eds.). 2015. Handbook of unmanned aerial vehicles. Springer, Netherlands.
- Van Auken, O. W. 2000. Shrub invasions of North American semiarid grasslands. *Annu. Rev. Ecol. Syst.* **31**, 197–215.
- Wulder, M., J. White, F. Alvarez, T. Han, J. Rogan, and B. Hawkes. 2009. Characterizing boreal forest wildfire with multi-temporal Landsat and LIDAR data. *Remote Sens. Environ.* **113**, 1540–1555.
- Xie, Y., Z. Sha, and M. Yu. 2008. Remote sensing imagery in vegetation mapping: a review. *J. Plant Ecol.* **1**, 9–23.
- Zarco-Tejada, P. J., V. González-Dugo, and J. A. Berni. 2012. Fluorescence, temperature and narrow-band indices acquired from a UAV platform for water stress detection using a micro-hyperspectral imager and a thermal camera. *Remote Sens. Environ.* **117**, 322–337.